

Cite this: DOI: 00.0000/xxxxxxxxxx

# Unraveling the Synergy between Metal-Organic Frameworks and Co-Catalysts in Photocatalytic Water Splitting<sup>†</sup>

Stefano Falletta,<sup>\*a</sup> Patrick Gono,<sup>a</sup> Zhendong Guo,<sup>a‡</sup> Stavroula Kampouri,<sup>b</sup> Kyriakos C. Stylianou,<sup>b¶</sup> and Alfredo Pasquarello<sup>a</sup>

Received Date

Accepted Date

DOI: 00.0000/xxxxxxxxxx

We investigate the synergy occurring in photocatalytic water splitting between the metal-organic framework MIL-125-NH<sub>2</sub> and two co-catalysts, namely NiO and Ni<sub>2</sub>P, by calculating their band edge alignment with respect to the redox levels of liquid water. For the NiO/H<sub>2</sub>O and Ni<sub>2</sub>P/H<sub>2</sub>O interfaces, we employ an explicit atomistic description of water and perform molecular dynamics simulations considering both molecular and dissociated water adsorbed at the co-catalyst surface. For the MIL-125-NH<sub>2</sub>/NiO and MIL-125-NH<sub>2</sub>/Ni<sub>2</sub>P interfaces, we rely on the concept of charge neutrality and use a scheme combining the electron affinities and the charge neutrality levels of the interface components. We provide a description of the underlying fundamental processes that is consistent with photoluminescence and intrinsic activity experiments and that supports NiO and Ni<sub>2</sub>P as suitable co-catalysts for MIL-125-NH<sub>2</sub> as far as the hydrogen evolution reaction is concerned.

## 1 Introduction

Photocatalysis has gained a lot of interest in recent years for its potential to produce energy in a clean and sustainable way.<sup>1–6</sup> Under suitable photocatalytic conditions, the photogenerated electron-hole pairs in the photocatalyst may activate the water splitting reaction, leading to the evolution of hydrogen. The use of a co-catalyst in conjunction with the photocatalyst can significantly enhance the photocatalytic activity of the system.<sup>7,8</sup> Indeed, co-catalysts can promote the separation of photogenerated electrons and holes, and provide catalytic centers for the water splitting reaction. The photocatalytic efficiency depends on the synergy between the photocatalyst and the co-catalyst, which is mainly determined by their band edge alignment, kinetic compatibility, and morphological match.<sup>8</sup> Identifying suitable co-catalysts for photocatalysts represents therefore a promising strategy for improving the efficiency of photocatalytic systems.

Metal-organic frameworks (MOFs) have been found to be ideal photocatalyst candidates, thanks to their structural versatility

and tunable optical properties.<sup>9–18</sup> A great deal of attention has been devoted to MIL-125-NH<sub>2</sub>, a MOF that shows a visible-light-induced activity for hydrogen production.<sup>7,15,19–21</sup> In this regards, Kampouri *et al.* have compared the synergy between several co-catalysts and the photocatalyst MIL-125-NH<sub>2</sub>.<sup>8</sup> They have shown that the highest performances are reached by two co-catalysts, namely NiO and Ni<sub>2</sub>P leading to hydrogen evolution rates of 1084 and 1230  $\mu\text{mol h}^{-1}\text{g}^{-1}$ , respectively.<sup>8</sup> A schematic representation of the two photocatalytic systems is illustrated in Fig. 1. To understand this synergy, photoluminescence experiments with various concentrations of co-catalyst nanoparticles were performed. It is observed that the light emission from the MOF quenches in the presence of Ni<sub>2</sub>P nanoparticles,<sup>8</sup> indicating that Ni<sub>2</sub>P prevents the carrier recombination process by withdrawing electrons from the photocatalyst. However, the light emission is only partially affected when measured in the presence of NiO nanoparticles,<sup>8</sup> suggesting that the electron transfer from MIL-125-NH<sub>2</sub> to NiO is less favorable than to Ni<sub>2</sub>P. Additionally, Kampouri *et al.* have measured the intrinsic activity for the hydrogen evolution reaction of the two co-catalysts, finding higher values for NiO than for Ni<sub>2</sub>P.<sup>8</sup> A theoretical explanation of these experimental findings is however still missing.

The photocatalytic synergy between MIL-125-NH<sub>2</sub> and the two co-catalysts is critically affected by the alignment of the band edges of NiO, Ni<sub>2</sub>P, and MIL-125-NH<sub>2</sub> with respect to the redox levels of liquid water. A favorable band alignment for the hydrogen evolution reaction is achieved when the conduction

<sup>a</sup> Chaire de Simulation à l'Echelle Atomique (CSEA), Ecole Polytechnique Fédérale de Lausanne (EPFL), CH-1015 Lausanne, Switzerland. E-mail: stefano.falletta@epfl.ch

<sup>b</sup> Laboratory of Molecular Simulation (LSMO), Institute of Chemical Sciences and Engineering, Ecole Polytechnique Fédérale de Lausanne (EPFL), CH-1951 Sion, Switzerland.

<sup>‡</sup> Present address: College of Energy, Soochow Institute for Energy and Materials Innovations (SIEMIS), Soochow University, Suzhou 215006, China.

<sup>¶</sup> Present address: Department of Chemistry, Oregon State University, Corvallis, OR 97331, USA.

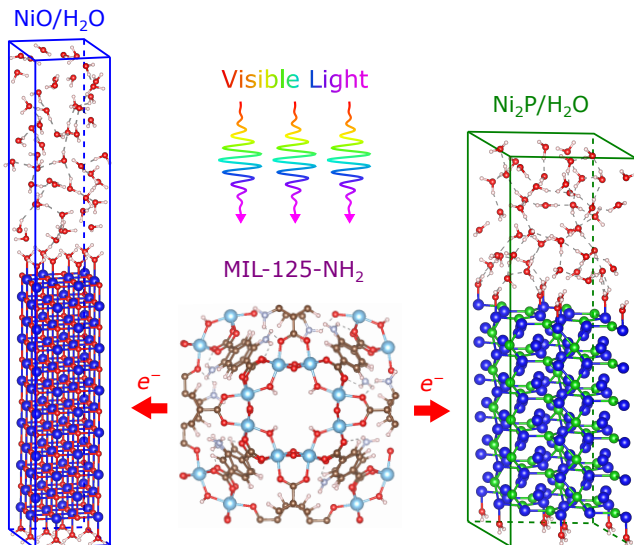


**Fig. 1** Schematic representation of the composite MIL-125-NH<sub>2</sub>/NiO/H<sub>2</sub>O and MIL-125-NH<sub>2</sub>/Ni<sub>2</sub>P/H<sub>2</sub>O photocatalytic interfaces. The photogenerated electrons in MIL-125-NH<sub>2</sub> are transferred to the co-catalyst (NiO, Ni<sub>2</sub>P) to promote the hydrogen evolution reaction.

band of the co-catalyst is higher than the hydrogen reduction potential ( $H^+/H_2$ ) and lower than the conduction band of the photocatalyst. Analogously, favorable thermodynamic conditions for the oxygen evolution reaction are reached when the valence band of the co-catalyst is lower than the water oxidation potential ( $O_2/H_2O$ ) and higher than the valence band of the photocatalyst.

Most of the work on the alignment of energy levels at semiconductor/water interfaces has been conducted using methods of various accuracy for modeling the interactions at the interface.<sup>22–35,35–39</sup> For instance, Castelli *et al.* used an empirical approach relating the band edges with the electronegativity of the material.<sup>22,23</sup> Stevanović *et al.* relied on the electron affinity model, neglecting the interactions at the interface.<sup>27</sup> Wu *et al.* used a nonequibrated interface model for semiconductor/water interfaces,<sup>29</sup> which did not account for the specific adsorption mechanism of the surface water molecules. For all these cases, it was shown that such methods may lead to significant errors, affecting the accuracy of the alignment.<sup>34</sup> This suggests that the interface with water needs to be accounted for at the atomistic level to achieve accurate results.<sup>34</sup> This is due to the fact that the orientation of the water dipoles at the semiconductor surface sensibly affects the alignment.<sup>34,40</sup> In this regard, the determination of the band edges of the semiconductor at the hybrid functional level has been extensively verified in previous literature.<sup>34,39,41</sup> In particular, from a variety of systems including semiconductor/water,<sup>34</sup> solid/solid,<sup>41</sup> and crystalline/amorphous interfaces,<sup>39</sup> it can be inferred that the accuracy of this method with respect to experiment amounts to  $\sim 0.20$  eV. A further complication to achieve the full alignment at the MOF/co-catalyst/water system is given by the poor characterization of the photocatalyst/co-catalyst interface. Indeed, not only the detailed bonding patterns but even the exposed surfaces at the interface are entirely unknown. This prevents the direct atomistic

modelling of the interface and requires the consideration of alignment schemes that are primarily based on the intrinsic properties of the bulk components.<sup>42</sup>

In this work, we investigate the role of NiO and Ni<sub>2</sub>P as co-catalysts for MIL-125-NH<sub>2</sub> by calculating the band edge alignment at the composite MIL-125-NH<sub>2</sub>/NiO/H<sub>2</sub>O and MIL-125-NH<sub>2</sub>/Ni<sub>2</sub>P/H<sub>2</sub>O interfaces. We model the NiO/H<sub>2</sub>O and Ni<sub>2</sub>P/H<sub>2</sub>O interfaces by using an explicit atomistic description of the solvent. In this regard, we consider both molecular and dissociated water adsorbed at the co-catalyst surface and determine the most stable configuration. For the alignment at the MIL-125-NH<sub>2</sub>/NiO and MIL-125-NH<sub>2</sub>/Ni<sub>2</sub>P interfaces, we rely on the concept of charge neutrality and use a scheme combining the electron affinities and the charge neutrality levels of the interface components.<sup>42</sup> We demonstrate that NiO and Ni<sub>2</sub>P can act as suitable co-catalysts for MIL-125-NH<sub>2</sub> in the case of the hydrogen evolution reaction. Moreover, our description provides a consistent interpretation of the photoluminescence and intrinsic activity experiments.<sup>8</sup>

## 2 Computational details

The calculations are performed with the CP2K suite of codes.<sup>43–46</sup> Goedecker-Teter-Hutter (GTH) pseudopotentials<sup>44,45</sup> are used to describe the electron core-valence interactions. Calculations are performed with MOLOPT Gaussian basis sets: double- $\zeta$  for Ni, O, P, H, C and N, and triple- $\zeta$  for Ti.<sup>47</sup> The Brillouin zone is sampled solely at the  $\Gamma$ -point. The energy cutoff for the plane waves is set to 800 Ry. The relaxed structures of bulk NiO, Ni<sub>2</sub>P and MIL-125-NH<sub>2</sub> (cf. Table 1) are obtained at the semilocal level of theory using the Perdew-Burke-Ernzerhof (PBE) functional<sup>48</sup> by converging the lattice parameters with respect to the supercell sizes. Angles and symmetries are kept fixed during the relaxation. The molecular dynamics (MD) simulations of the co-catalyst/water interfaces are performed at the PBE functional level. For specific tasks, we also resort to hybrid functionals of the form PBE0( $\alpha$ ),<sup>49</sup> where  $\alpha$  is the fraction of Fock exchange. We employ the auxiliary density matrix method (ADMM)<sup>46</sup> to speed up the hybrid functional calculations. The fraction  $\alpha$  in the PBE0( $\alpha$ ) functional is set to 0.22 in the case of NiO and to 0.50 in the case of Ni<sub>2</sub>P in order to reproduce their respective experimental energy gaps of 4.3 eV<sup>50</sup> and 1.0 eV.<sup>51</sup> In the case of MIL-125-NH<sub>2</sub>, we use  $\alpha = 0.35$ , which complies with Koopmans' condition<sup>52</sup> and gives a fundamental band gap of 4.25 eV.

In the MD simulations, the van der Waals interactions are modeled through the rVV10 functional.<sup>53,54</sup> A Nosé-Hoover thermostat is used to sample the NVT ensemble.<sup>55,56</sup> The temperature is kept at 350 K to ensure a frank diffusive motion of liquid water.<sup>34</sup> The time step in the MD is set to 0.5 fs. We also perform MD simulations at the hybrid functional level. In this case, we still describe van der Waals interactions through a nonlocal rVV10 functional, but adapt the  $b$  parameter to ensure that the equilibrium density of liquid water remains fixed at 1 g·cm<sup>-3</sup>.<sup>57,58</sup> Previous studies have shown that the structure of liquid water remains very similar provided this condition is satisfied.<sup>57,58</sup> Thus, for a given PBE0( $\alpha$ ) functional, we obtain the value of  $b$  through lin-

ear interpolation between 9.3 and 5.3, which pertain to PBE and PBE0(0.40), respectively.<sup>57,58</sup> Hence, the onset of hybrid functional interactions upon the equilibration of the structure at the PBE level is not expected to cause any major structural reorganization in the water layer and should capture the reorientation of the water molecules in the first water layer attached to the co-catalyst on a relatively short time scale.

The main computational cost of the calculations performed in this work is represented by the MD simulations of the co-catalyst/water interface models, each of which contains  $\sim 400$  atoms. In total, we performed  $\sim 40$  ps of MD at the PBE semilocal functional level, which corresponds to the computational cost of 80'000 steps of atomic relaxation. Furthermore, the MD simulations performed at the hybrid functional level imply an additional cost equivalent to that globally spent for the semilocal simulations.

**Table 1** Lattice parameters (in Å) of NiO, Ni<sub>2</sub>P and MIL-125-NH<sub>2</sub> compared with their experimental values.<sup>15,50,51,59,60</sup>

		Present	Expt.
NiO	<i>a</i>	4.207	4.168
	<i>c</i>	3.383	3.387
Ni <sub>2</sub> P	<i>a</i>	5.880	5.865
	<i>c</i>	17.890	18.172

### 3 Alignment at the co-catalyst/water interfaces

In Fig. 2, we illustrate the procedure to calculate the energy alignment at co-catalyst/water interfaces using an explicit solvent model.<sup>34–39</sup> First, one determines the valence and conduction band edges with respect to the time-averaged electrostatic potential  $V_{\text{co-cat}}$  in the bulk co-catalyst. Second, one positions the redox level  $\mu_{\text{H}^+/\text{H}_2}$  of the hydrogen evolution reaction with respect to the time-averaged electrostatic potential  $V_{\text{w}}$  in bulk water. Finally, the potential offset  $\Delta V = V_{\text{w}} - V_{\text{co-cat}}$  between the co-catalyst and the water layer is calculated.

Before addressing the potential line-up at the co-catalyst/water interfaces, we focus on the relevant electronic levels of the interface components. The band edges of NiO and Ni<sub>2</sub>P are found to be converged for supercells of size  $4 \times 4 \times 4$  and  $3 \times 3 \times 6$ , respectively. We neglect thermal effects on the band edges. For NiO, the arrangement of the magnetic spins in our NiO supercell is antiferromagnetic, in agreement with the experimental evidence.<sup>61</sup> The obtained values are reported in Table 2. For the alignment of the redox levels of bulk water, we take the position of the standard hydrogen electrode (SHE) at 0.87 eV below the average electrostatic potential of bulk water following previous work in which this level was determined.<sup>62</sup>

In the following, we apply a multi-step procedure for determining the potential offset  $\Delta V$ , which consists in (i) performing MD simulations of the explicit interfaces of the co-catalysts with water at the semi-local functional level and (ii) extracting the potential offset from these MD simulations.<sup>25,35,36,38,39,63–65</sup> The alignment is then achieved as illustrated in Fig. 2(a). In this work, (iii) we additionally estimate the energy shift resulting from the

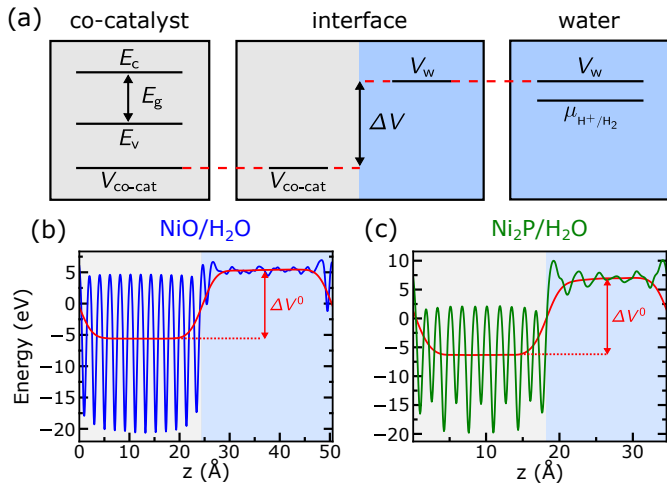


**Fig. 2** (a) Schematic representation of the band edge alignment at the co-catalyst/water interface. The alignment procedure between the energy levels in the co-catalyst and in water is shown in red. The average electrostatic potential is shown for the most stable MD at the (b) NiO/H<sub>2</sub>O and (c) Ni<sub>2</sub>P/H<sub>2</sub>O interfaces. The electrostatic potential is averaged over the directions parallel to the interfaces and over time. In practice, the three-dimensional electrostatic potential is first averaged over the planes parallel to the interface, resulting into a one-dimensional potential along  $z$  for each step of the MD. Next, such one-dimensional potentials are averaged over time along the equilibrated trajectories of the MD. The red line corresponds to a Gaussian-based convolution.

**Table 2** Valence band (VB) and conduction band (CB) referred to the average electrostatic potential in bulk NiO and Ni<sub>2</sub>P, and standard hydrogen electrode (SHE) level with respect to the average electrostatic potential in bulk water. All energies are in eV.

	VB	CB	SHE
NiO	8.23	12.53	–
Ni <sub>2</sub> P	12.23	13.23	–
H <sub>2</sub> O	–	–	–0.87 <sup>62</sup>

reorientation of the surface water molecules upon the use of the hybrid functional PBE0( $\alpha$ ) going beyond the semilocal PBE functional. The good agreement with the experiment achieved by Guo *et al.* with PBE structures suggests that such corrections are smaller than the overall accuracy of the method ( $\sim 0.2$  eV).<sup>34</sup> Nevertheless, we explicitly account for this shift as a refinement of our results. Finally, (iv) an energy shift has to be applied to achieve the potential offset at pH = 0.<sup>25,34,35</sup>

In the experiments of Kampouri *et al.*,<sup>8</sup> the NiO and Ni<sub>2</sub>P nanoparticles are physically mixed with the crystalline powder of MIL-125-NH<sub>2</sub>. These nanoparticles have sizes around 10–20 nm<sup>8</sup> and are thus large enough to be considered as bulk structures in supercell calculations. Therefore, the band alignment of these nanoparticles with water can be performed through the use of slabs, which are suitable to achieve the band alignment between bulk materials. We construct our model by taking six-layer slabs, with a surface repeat unit of  $2 \times 2$ , interfaced with liquid water in a set-up satisfying periodic boundary conditions. The slabs are assembled along the directions (001) and (0001) for NiO and Ni<sub>2</sub>P, respectively, with the Ni<sub>2</sub>P slab terminated by Ni<sub>3</sub>P<sub>2</sub> surfaces. Indeed, in the case of NiO, it is found that the (001) sur-

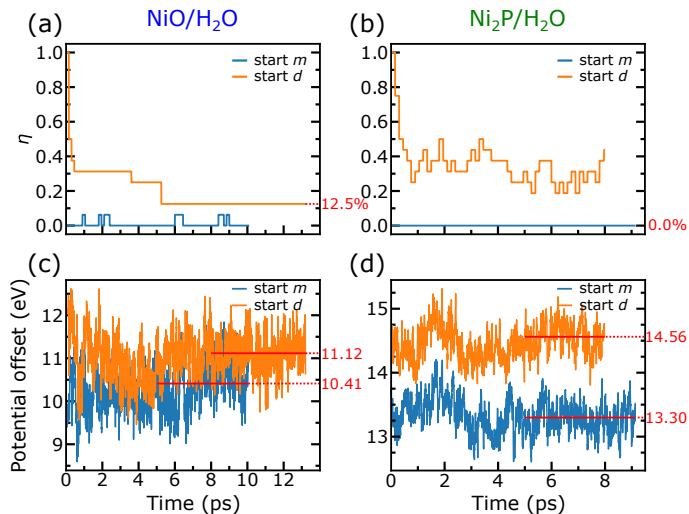


**Fig. 3** Time evolution of the dissociation fraction  $\eta$  at the (a) NiO/H<sub>2</sub>O and (b) Ni<sub>2</sub>P/H<sub>2</sub>O interfaces. Time evolution of the potential offset at the (c) NiO/H<sub>2</sub>O and (d) Ni<sub>2</sub>P/H<sub>2</sub>O interfaces. The two MD simulations for each interface are initialized with molecular (*m*) or dissociated (*d*) water at the surface. The values of  $\Delta V^0$  averaged over the equilibrated trajectories are denoted with horizontal red lines.

face is the most stable crystal plane.<sup>66</sup> This is also the case for other rocksalt materials and this facet is generally found to dominate in the crystal growth.<sup>67,68</sup> In the case of Ni<sub>2</sub>P, it has been found that the nanoparticles used for the hydrogen evolution reaction exhibit a high density of exposed (0001) facets.<sup>69</sup> Along the direction (0001), Ni<sub>2</sub>P is characterized by the alternation of Ni<sub>3</sub>P and Ni<sub>3</sub>P<sub>2</sub> planes. In this regard, Li *et al.* have shown that the most stable surfaces of Ni<sub>2</sub>P terminate with Ni<sub>3</sub>P<sub>2</sub> planes.<sup>70</sup> Additionally, He *et al.* studied the surface stability and the equilibrium crystal morphology of Ni<sub>2</sub>P nanoparticles and found that the (0001) Ni<sub>3</sub>P<sub>2</sub> surfaces are the most stable surfaces compared to other facets.<sup>71</sup>

The sizes of the co-catalyst slabs guarantee that the average electrostatic potential in the co-catalyst converges within 0.1 eV, as ascertained in test calculations for slabs in vacuum. The water bulk layer contains 50 and 46 water molecules in the NiO/H<sub>2</sub>O and Ni<sub>2</sub>P/H<sub>2</sub>O model systems, respectively. These models ensure a correct description of the density and the structural properties of water in the central region of the water layer (*vide infra*). The size of the NiO/H<sub>2</sub>O and Ni<sub>2</sub>P/H<sub>2</sub>O interfaces can also easily be inferred from Figs. 2(b) and (c), where we illustrate the time-averaged electrostatic potential at these interfaces.

### 3.1 Molecular dynamics simulations

For each interface, we run MD simulations with two distinct initial configurations at the surface, showing either molecular or dissociated water.<sup>25,34</sup> In the molecular configuration (*m*), the water molecules are attached to the co-catalyst surface through metal-O bonds. In the dissociated configuration (*d*), the OH group forms a bond with the metal atom and H is bonded to the non-metal atom.

We monitor the behavior of the surface water molecules dur-

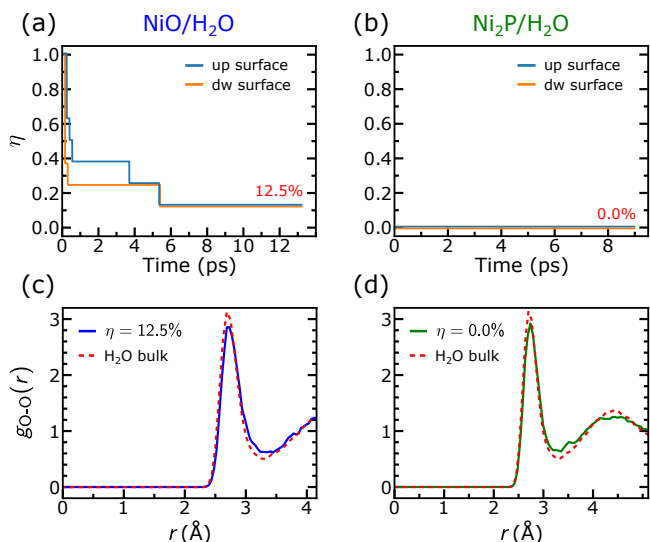


**Fig. 4** Time evolution of the dissociation fraction  $\eta$  for both top and bottom co-catalyst surfaces at the (a) NiO/H<sub>2</sub>O and (b) Ni<sub>2</sub>P/H<sub>2</sub>O interfaces. Oxygen-oxygen radial distribution function  $g_{O-O}(r)$  of bulk water in the (c) NiO/H<sub>2</sub>O and (d) Ni<sub>2</sub>P/H<sub>2</sub>O interfaces compared with the  $g_{O-O}(r)$  of bulk liquid water. For the co-catalyst/water interfaces, the  $g_{O-O}(r)$  is calculated in an inner region of the water layer defined by a thickness of 5 Å.

ing the MD by calculating the fraction  $\eta$  of dissociated water molecules over the total number of water molecules adsorbed at the co-catalyst surface. In all the MD runs, the value of  $\eta$  stabilizes after an equilibration time of about 5 ps. However, as illustrated in Figs. 3(a) and (b), we find that for both the NiO/H<sub>2</sub>O and Ni<sub>2</sub>P/H<sub>2</sub>O interfaces the dissociation fractions do not converge to the same value when starting from the two initial configurations considered. However, in all cases, the achieved values of  $\eta$  are the same at the two co-catalyst surfaces occurring in our simulation cell, as illustrated in Figs. 4(a) and (b). Moreover, we calculate the O-O radial distribution function  $g_{O-O}(r)$  in the bulk-like region of the water layer. We obtain a good agreement between the  $g_{O-O}(r)$  calculated at the co-catalyst/water interfaces and in bulk water, as shown in Figs. 4(c) and (d).

### 3.2 Potential offset at the co-catalyst/water interfaces

We illustrate in Figs. 3(c) and (d) the potential offset  $\Delta V^0$  as calculated at the semilocal level for the NiO/H<sub>2</sub>O and Ni<sub>2</sub>P/H<sub>2</sub>O interfaces. To identify the right value of  $\Delta V^0$ , we need to assess the relative stability of the surface water molecules in the equilibrated configurations of the two MD runs. In Fig. 5, we show the time evolution of the potential energy during the MD simulations. For NiO/H<sub>2</sub>O, we find that the configuration with  $\eta = 12.5\%$  is energetically more stable by 0.29 eV per surface water molecule on average. On the other hand, for Ni<sub>2</sub>P/H<sub>2</sub>O, the configuration with  $\eta = 0\%$  is energetically more stable by 0.38 eV per surface water molecule on average. Considering the large difference in stability between the MD simulations initialized with either molecular or dissociated surface water molecules, we extend the durations only for the most stable simulations.

To take into account entropic effects, we compute the thermo-

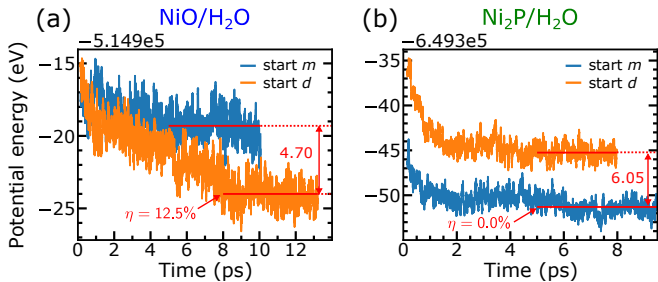


**Fig. 5** Time evolution of the potential energy at the (a) NiO/H<sub>2</sub>O and (b) Ni<sub>2</sub>P/H<sub>2</sub>O interfaces. The two MD simulations for each interface are initialized with molecular (*m*) or dissociated (*d*) water at the surface. The potential energy values averaged over the equilibrated trajectories are denoted with horizontal red lines. The dissociation fractions  $\eta$  of the most stable trajectories are indicated.

dynamic corrections for a single water molecule at the NiO and Ni<sub>2</sub>P surfaces, in the *m* and *d* configurations. We approximate the thermodynamic corrections as:  $\Delta G = \text{ZPE} - TS + \Delta U_{0 \rightarrow T}$ , where ZPE is the vibrational zero point energy, *S* the vibrational entropy, and  $\Delta U_{0 \rightarrow T}$  the contribution to the internal energy due to the finite temperature *T*.<sup>72</sup> We assume the vibrational spectrum of the substrate to be unperturbed by the adsorbate, and hence compute the vibrational spectrum of the adsorbate while keeping the substrate frozen. In Table 3, we show the thermodynamic corrections obtained for a single water molecule either molecularly or dissociatively adsorbed at the NiO and Ni<sub>2</sub>P surfaces. We find corrections smaller than 0.03 eV per water molecule, thereby indicating that entropic contributions of molecular or dissociated surface water are very similar. As a consequence, we conclude that the most stable structures of the NiO/H<sub>2</sub>O and Ni<sub>2</sub>P/H<sub>2</sub>O interfaces show a dissociation fraction of 12.5% and 0%, respectively. From the corresponding equilibrated trajectories, we determine the time-averaged potential offset  $\Delta V^0$  (cf. Fig. 2).

**Table 3** Thermodynamic corrections for a single water molecule adsorbed on the NiO and Ni<sub>2</sub>P surfaces, in the molecular (*m*) and in the dissociated (*d*) configurations. All energies are in eV.

Material	Config.	ZPE	$-TS$	$\Delta U_{0 \rightarrow T}$	$\Delta G$
NiO	<i>m</i>	0.66	-0.17	0.09	0.58
	<i>d</i>	0.65	-0.13	0.08	0.60
Ni <sub>2</sub> P	<i>m</i>	0.65	-0.20	0.10	0.55
	<i>d</i>	0.56	-0.12	0.08	0.52

### 3.3 Hybrid functional corrections

Hybrid functionals are expected to yield structures of higher accuracy compared to semilocal functionals, but reaching fully equilibrated configurations at this higher level of theory is computationally prohibitive. Nevertheless, it is possible to capture the reorientation of the water molecules occurring on relatively short time scales that such functionals would induce. To this end, we perform 1.5 ps of MD with the PBE0( $\alpha$ ) functional starting from the most stable structures equilibrated at the PBE level. We fix the fraction of exact exchange at 0.22 and 0.50 for the NiO/H<sub>2</sub>O and Ni<sub>2</sub>P/H<sub>2</sub>O interfaces, respectively, in order to reproduce the band gaps of the two co-catalysts. Since typical reorientation times are

on the order of tens of femtoseconds, a MD with a duration of 1.5 ps is expected to capture the dipole reorientations of the surface water molecules. As described in Section 2, the structural properties of bulk water are preserved through the combined adjustment of the fraction  $\alpha$  of Fock exchange and of the *b* parameter of the nonlocal rVV10 functional.

We estimate the correction  $\Delta_{\text{hyb}}$  due to the dipole reorientation of the surface water molecules as follows. First, we infer through proper time averages the angles  $\theta_0$  and  $\theta_\alpha$  between the axis of the surface water molecules and the direction orthogonal to the interface in the PBE and PBE0( $\alpha$ ) MD simulations, respectively (cf. Table 4). We remark that these angles are found to converge rapidly on the scale of the simulations, as they weakly depend on the long-range relaxations in the water layer occurring on longer time-scales. Since the orientation of the water molecules in the first water layer have been found to dominate the alignment at the co-catalyst-water interface,<sup>40</sup> we evaluate the effect of the reorientation of the water molecules on the alignment with respect to the vacuum level by considering co-catalyst/vacuum models in which a single water layer with fixed orientations occurs at the interface. These calculations give corrections of  $\Delta_{\text{hyb}} = -0.14$  eV and  $\Delta_{\text{hyb}} = -0.24$  eV for NiO and Ni<sub>2</sub>P, respectively. These corrections are overall very small and comparable with the accuracy of the method based on PBE structures. This is consistent with the agreement with experiment achieved by Guo *et al.*<sup>34</sup> The effect is found to be slightly larger in the case of Ni<sub>2</sub>P for which the use of the PBE0( $\alpha$ ) functional leads to the opening of the band gap. We account for these corrections in the potential offset  $\Delta V^0$ .

**Table 4** Average angles  $\theta_0$  and  $\theta_\alpha$  formed by the surface water dipoles with respect to the direction orthogonal to the interface during the MD simulations performed with the PBE and PBE0( $\alpha$ ) functionals, respectively, for both the NiO/H<sub>2</sub>O and Ni<sub>2</sub>P/H<sub>2</sub>O interfaces. The angular reorientation is given by  $\Delta\theta$ .

	$\theta_0$	$\theta_\alpha$	$\Delta\theta$
NiO/H <sub>2</sub> O	65.8°	63.3°	-2.5°
Ni <sub>2</sub> P/H <sub>2</sub> O	56.6°	50.9°	-5.7°

### 3.4 pH energy shift

The interfaces considered in this work are neutral by construction, and hence the aqueous environment is found at the pH corresponding to the zero point charge (ZPC). Therefore, the energy levels obtained from the MD simulations pertain to the pH of ZPC. However, our aim is to refer them with respect to the zero pH condition of the SHE. This requires applying an energy shift  $\Delta_{\text{pH}}$  to the potential offset between the co-catalyst and the water layer. Considering that the conduction and valence bands of semiconductors generally show a Nernstian behavior at the interface with water,<sup>73–76</sup> we can calculate the energy shift as  $\Delta_{\text{pH}} = 0.059 \text{ eV} \cdot \text{pH}_{\text{ZPC}}$ . For NiO, the experimental  $\text{pH}_{\text{ZPC}}$  is found to be 8.4.<sup>77</sup> For Ni<sub>2</sub>P, no experimental values for  $\text{pH}_{\text{ZPC}}$  are reported in the literature. Considering that a variation of the pH by one unit leads to a correction of only 0.059 eV, we can reasonably approximate  $\text{pH}_{\text{ZPC}}$  of Ni<sub>2</sub>P by 8.4, as in the case of NiO. We account for  $\Delta_{\text{pH}}$  in the potential offset  $\Delta V^0$ .

## 4 Alignment at the photocatalyst/co-catalyst interfaces

The alignment at the photocatalyst/co-catalyst interface can be performed relying on the establishment of charge neutrality in semiconductors.<sup>31,42</sup> In this way, the alignment at the interface is mainly affected by the band structures of the interface components and the difficulty of modelling the interface at the atomic scale is overcome.<sup>31,42,78–82</sup> It has been shown that the alignment between two semiconductors depends on the presence of dipoles at their interface as in the case of Schottky barriers.<sup>42,83–85</sup> When no charge transfer dipoles are formed at the interface, the conduction band offset can be calculated as the difference between the electron affinities of the two semiconductors, as prescribed by the electron affinity model.<sup>86</sup> The presence of dipoles modifies the band alignment at the interface, which then results from the interplay between the electron affinities and the charge neutrality levels of the interface components.<sup>42</sup> In particular, the offset  $\phi$  between the conduction bands of two semiconductors  $a$  and  $b$  can be calculated as:<sup>42</sup>

$$\phi = (\chi_a - \Phi_{\text{CNL},a}) - (\chi_b - \Phi_{\text{CNL},b}) + S(\Phi_{\text{CNL},a} - \Phi_{\text{CNL},b}) \quad (1)$$

where  $\chi_a$  and  $\chi_b$  are the electron affinities pertaining to the surfaces of interest,  $\Phi_{\text{CNL},a}$  and  $\Phi_{\text{CNL},b}$  are the charge neutrality levels referred to the vacuum level, and  $S$  is the Schottky pinning factor of the semiconductor with the larger band gap at the interface. Mönch showed that the  $S$  parameter can be empirically related to the optical dielectric constant  $\epsilon_\infty$  of the semiconductor via the following relationship:<sup>87,88</sup>

$$S = \frac{1}{1 + 0.1(\epsilon_\infty - 1)^2} \quad (2)$$

For wide gap semiconductors,  $S$  is generally close to 1, because of the small  $\epsilon_\infty$ . When  $S = 1$ , the alignment procedure illustrated in Eq. (1) falls back on the electron affinity model. The charge neutrality level (CNL) is a measure of the mean electronegativity of the semiconductor and can be determined as the energy at which the following Green's function  $G$  is equal to zero:<sup>42</sup>

$$G(E) = \int_{\text{BZ}} \frac{N(E')dE'}{E - E'} \quad (3)$$

where  $N(E)$  is the density of states (DOS). From Eq. (3) we see that the CNL is a weighted average over the DOS: the higher the DOS in the valence band, the more the CNL is pushed towards the conduction band and viceversa.

### 4.1 Electron affinities

We show in Fig. 6 the procedure to determine the electron affinities of NiO, Ni<sub>2</sub>P and MIL-125-NH<sub>2</sub>. For NiO and Ni<sub>2</sub>P, we interface our bulk models with vacuum and determine the position of the band structure with respect to the vacuum level by focusing on the average electrostatic potential across the slab. We use supercell sizes of 4×4×4 and 3×3×6 for NiO and Ni<sub>2</sub>P, respectively. The Ni<sub>2</sub>P slab is terminated by Ni<sub>3</sub>P<sub>2</sub> surfaces. For MIL-125-NH<sub>2</sub>, we calculate the vacuum level as the average electrostatic poten-

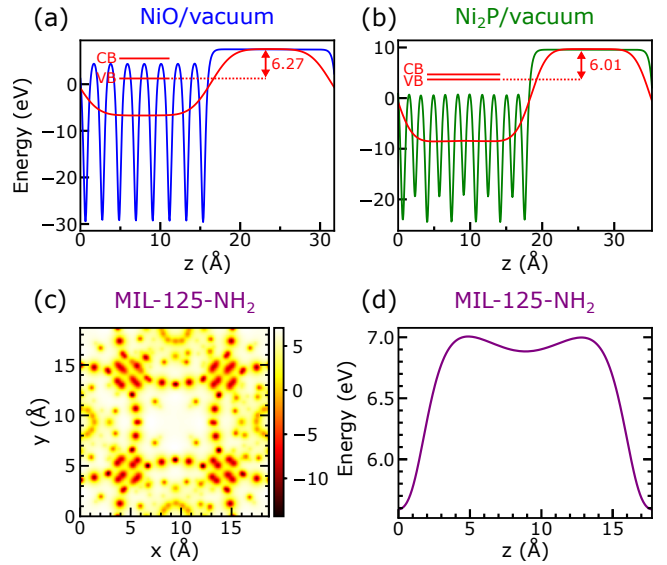


**Fig. 6** (a,b) Calculation of the electron affinities of NiO and Ni<sub>2</sub>P. The red line corresponds to a Gaussian-based convolution, while the horizontal lines indicate the valence band (VB) and conduction band (CB) of the bulk system referred to the average electrostatic potential in the inner region of the co-catalyst slab. (c) Electrostatic potential in MIL-125-NH<sub>2</sub> averaged over the direction  $z$ . (d) Electrostatic potential in MIL-125-NH<sub>2</sub> along the line parallel to  $z$  and intersecting the plane  $xy$  at the center of the pore. In (c) and (d), the energies are referred to the valence band of MIL-125-NH<sub>2</sub>. The presence of a plateau in (d) at the center of the pore ( $z = 8.8 \text{ \AA}$ ) justifies the choice of averaging the electrostatic potential over a sphere with a radius of  $2 \text{ \AA}$  to determine the vacuum level. In this way, the valence band of MIL-125-NH<sub>2</sub> is found to lie  $6.84 \text{ eV}$  below the vacuum level.

tial at the center of the pore.<sup>89</sup> The reference value is obtained as an average over a sphere with a radius of  $2 \text{ \AA}$ .

### 4.2 Charge neutrality levels

In Fig. 7, we illustrate the density of states and the charge neutrality levels for NiO, Ni<sub>2</sub>P and MIL-125-NH<sub>2</sub>. We use supercell sizes of 4×4×4 and 3×3×6 for NiO and Ni<sub>2</sub>P, respectively. Moreover, using Eq. (2), we find  $S = 0.75$  for MIL-125-NH<sub>2</sub> ( $\epsilon_\infty = 2.84$ <sup>52</sup>), which corresponds to the interface component with the larger band gap.

The calculated electron affinities and charge neutrality levels referred to the vacuum level are given in Table 5. Using Eq. (1), we find that the conduction band of MIL-125-NH<sub>2</sub> lies  $0.03 \text{ eV}$  below the conduction band of NiO and  $2.61 \text{ eV}$  above the conduction band of Ni<sub>2</sub>P.

**Table 5** Electron affinity (EA), charge neutrality level (CNL), and average electrostatic potential (AEP) of NiO, Ni<sub>2</sub>P and MIL-125-NH<sub>2</sub> referred to the vacuum level. All energies are in eV.

	EA	CNL	AEP
NiO(001)	2.02	2.40	14.55
Ni <sub>2</sub> P(0001)	4.85	3.19	18.08
MIL-125-NH <sub>2</sub>	2.59	4.57	10.37

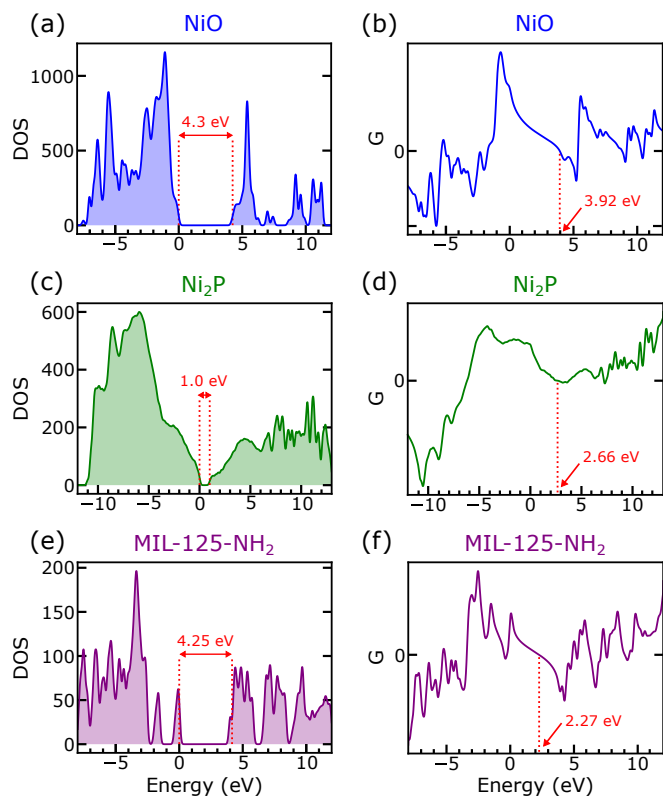
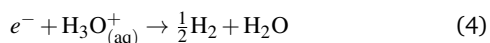


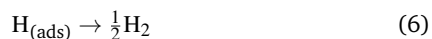
**Fig. 7** Density of states (DOS) and Green's function  $G$  in Eq. (3) of NiO (a,b), Ni<sub>2</sub>P (c,d) and MIL-125-NH<sub>2</sub> (e,f). The charge neutrality level is defined as the energy at which  $G = 0$ . The energies are referred to the valence band maxima of the bulk systems. The Gaussian broadening applied to the DOS has a width  $\sigma = 0.1$  eV.

## 5 Discussion and conclusions

The hydrogen evolution reaction reads



where the initial state is given by an electron in the conduction band and  $\text{H}_3\text{O}^+$  in the aqueous solution, and the final state is represented by the  $\text{H}_2$  gas. This reaction is exothermic as long as the energy of the conduction-band electron is higher than the redox level of the hydrogen evolution reaction (SHE). Additionally, we consider the intermediate state involving an adsorbed H atom  $\text{H}_{(\text{ads})}$ . The full reaction can then be described by a sequence of two reactions:



The first of these two reactions defines the redox level of the intermediate state and is exothermic as long as the conduction-band electron is higher than this redox level. To assess the position of the redox level pertaining to the intermediate state with respect to the final state, we use the computational hydrogen electrode method<sup>90,91</sup> to determine the Gibbs free energy of hydrogen adsorption  $\Delta G_{\text{H}}$  applied to our co-catalyst-water interfaces. We find  $\Delta G_{\text{H}} = 1.05$  eV and  $\Delta G_{\text{H}} = 0.51$  eV in the cases of NiO and Ni<sub>2</sub>P, re-

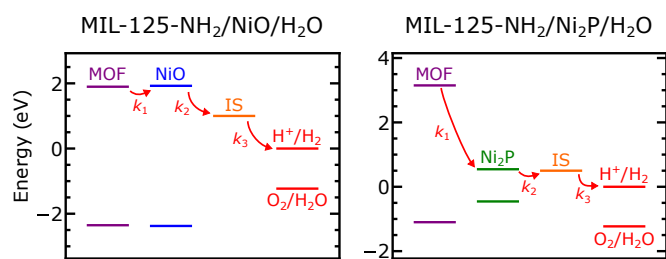


**Fig. 8** Alignment of the band edges at the composite MIL-125-NH<sub>2</sub>/NiO/H<sub>2</sub>O and MIL-125-NH<sub>2</sub>/Ni<sub>2</sub>P/H<sub>2</sub>O interfaces at pH = 0.  $k_1$  and  $k_2$  are the electron transfer rates from the photocatalyst to the co-catalyst and from the co-catalyst to the intermediate state (IS), respectively, while  $k_3$  is the reaction rate from the intermediate state to the SHE level.

spectively. We remark that in both cases  $\Delta G_{\text{H}}$  is positive, meaning that the desorption is an exothermic process. The position of the redox level pertaining to the intermediate state is found at an energy which is higher than the SHE by  $\Delta G_{\text{H}}$ . The resulting energy level alignments of the band edges at the MIL-125-NH<sub>2</sub>/NiO/H<sub>2</sub>O and MIL-125-NH<sub>2</sub>/Ni<sub>2</sub>P/H<sub>2</sub>O interfaces are shown in Fig. 8. Remarkably, we find that, within the accuracy of our calculations, the conduction bands of both NiO and Ni<sub>2</sub>P are favorably positioned with respect to the conduction band of MIL-125-NH<sub>2</sub> to operate as co-catalysts as far as the hydrogen evolution reaction is concerned. In the cases of both NiO and Ni<sub>2</sub>P, the intermediate state level falls between the conduction band of the co-catalyst and the SHE level, thereby enabling a cascade reaction leading to hydrogen evolution. This is in agreement with the experimental evidence.<sup>8</sup>

The band alignment is instrumental to understand the kinetics of the reactions between the photocatalyst, the co-catalyst and water. The two reactions from the photocatalyst to the co-catalyst and from the co-catalyst to the intermediate state involve electron transfer, and can therefore be described through Marcus theory.<sup>92</sup> According to Marcus theory,<sup>92</sup> the energy difference between the donor and the acceptor levels represents the driving force for the electron transfer. It is expected that the electron transfer rate from the co-catalyst to water can be described within the regular Marcus regime.<sup>93</sup> Hence, the larger the difference between the two energy levels, the higher the reaction rate associated. At variance, the reaction between the intermediate state and the SHE does not involve any electron transfer. However, according to the Bronsted-Evans-Polanyi principle,<sup>94</sup> it still holds that the higher the energy difference between the final and the initial state, the higher the reaction rate.

Our results then provide a consistent interpretation of the experimental results.<sup>8</sup> We denote by  $k_1$  and  $k_2$  the electron transfer rates from the photocatalyst to the co-catalyst and from the co-catalyst to the intermediate state, and by  $k_3$  the reaction rate from the intermediate state to the SHE level. The proximity of the conduction bands of MIL-125-NH<sub>2</sub> and NiO determines a low rate  $k_1$  (NiO), which underlies the persistence of the MOF photoluminescence in the MIL-125-NH<sub>2</sub>/NiO system. On the other hand, we find that  $k_1$  (Ni<sub>2</sub>P)  $>$   $k_1$  (NiO), which explains the quench of the

MOF photoluminescence in the MIL-125-NH<sub>2</sub>/Ni<sub>2</sub>P system. The characterization of the intrinsic photocatalytic activity of NiO and Ni<sub>2</sub>P carried out by Kampouri *et al.*<sup>8</sup> can be interpreted by considering the rates  $k_2$  and  $k_3$ . Indeed, according to our alignment,  $k_2(\text{NiO}) > k_2(\text{Ni}_2\text{P})$  and  $k_3(\text{NiO}) > k_3(\text{Ni}_2\text{P})$ , which supports an intrinsic photocatalytic activity in NiO larger than in Ni<sub>2</sub>P. Moreover, the higher activity of NiO could also be related to the partial dissociation of water molecules at the surface.<sup>95</sup> Hence, our analysis demonstrates that the MIL-125-NH<sub>2</sub>/NiO/H<sub>2</sub>O and MIL-125-NH<sub>2</sub>/Ni<sub>2</sub>P/H<sub>2</sub>O systems are subject to different combinations of favorable and unfavorable processes, suggesting that their overall similar photocatalytic performances result from a balance of compensating effects.

In conclusion, we addressed the role of NiO and Ni<sub>2</sub>P as co-catalysts in conjunction with MIL-125-NH<sub>2</sub>. We explained the observed synergy of NiO and Ni<sub>2</sub>P with MIL-125-NH<sub>2</sub> in terms of the band alignment between the catalyst, co-catalysts, and water. Our work sheds light onto the fundamental processes underlying the photocatalytic performance of a combined MOF/co-catalyst system, thereby establishing a theoretical methodology for identifying the optimal combinations of the components involved.

## Conflicts of interest

There are no conflicts to declare.

## Acknowledgements

We acknowledge useful interactions with Maria Fumanal and Francesco Ambrosio. This work has been realized in relation to the National Center of Competence in Research (NCCR) "Materials' Revolution: Computational Design and Discovery of Novel Materials (MARVEL)" of the SNSF. The calculations have been performed at the Swiss National Supercomputing Centre (CSCS) (grant under project IDs mr25 and s879) and at SCITAS-EPFL.

## Notes and references

- 1 A. Fujishima and K. Honda, *Nature*, 1972, **238**, 37.
- 2 S. U. Khan, M. Al-Shahry and W. B. Ingler, *Science*, 2002, **297**, 2243–2245.
- 3 A. Kudo and Y. Miseki, *Chem. Soc. Rev.*, 2009, **38**, 253–278.
- 4 M. G. Walter, E. L. Warren, J. R. McKone, S. W. Boettcher, Q. Mi, E. A. Santori and N. S. Lewis, *Chem. Rev.*, 2010, **110**, 6446–6473.
- 5 J. Liu, Y. Liu, N. Liu, Y. Han, X. Zhang, H. Huang, Y. Lifshitz, S.-T. Lee, J. Zhong and Z. Kang, *Science*, 2015, **347**, 970–974.
- 6 J. Luo, J.-H. Im, M. T. Mayer, M. Schreier, M. K. Nazeeruddin, N.-G. Park, S. D. Tilley, H. J. Fan and M. Grätzel, *Science*, 2014, **345**, 1593–1596.
- 7 Y. Horiuchi, T. Toyao, M. Saito, K. Mochizuki, M. Iwata, H. Higashimura, M. Anpo and M. Matsuoka, *J. Phys. Chem. C*, 2012, **116**, 20848–20853.
- 8 S. Kampouri, T. N. Nguyen, M. Spodaryk, R. G. Palgrave, A. Züttel, B. Smit and K. C. Stylianou, *Adv. Funct. Mater.*, 2018, **28**, 1806368.
- 9 T. Zhang and W. Lin, *Chem. Soc. Rev.*, 2014, **43**, 5982–5993.
- 10 M. Ranocchiari and J. A. van Bokhoven, *Phys. Chem. Chem. Phys.*, 2011, **13**, 6388–6396.
- 11 M. A. Nasalevich, C. H. Hendon, J. G. Santaclara, K. Svane, B. Van Der Linden, S. L. Veber, M. V. Fedin, A. J. Houtepen, M. A. Van Der Veen, F. Kapteijn *et al.*, *Sci. Rep.*, 2016, **6**, 23676.
- 12 J. Santaclara, F. Kapteijn, J. Gascon and M. van der Veen, *CrystEngComm*, 2017, **19**, 4118–4125.
- 13 J. G. Santaclara, M. A. Nasalevich, S. Castellanos, W. H. Evers, F. C. Spoor, K. Rock, L. D. Siebbeles, F. Kapteijn, F. Grozema, A. Houtepen *et al.*, *ChemSusChem*, 2016, **9**, 388–395.
- 14 H. Liu, C. Xu, D. Li and H.-L. Jiang, *Angew. Chem.*, 2018, **57**, 5379–5383.
- 15 C. H. Hendon, D. Tiana, M. Fontecave, C. Sanchez, L. D'arras, C. Sassoie, L. Rozes, C. Mellot-Draznieks and A. Walsh, *J. Am. Chem. Soc.*, 2013, **135**, 10942–10945.
- 16 S. Pullen, H. Fei, A. Orthaber, S. M. Cohen and S. Ott, *J. Am. Chem. Soc.*, 2013, **135**, 16997–17003.
- 17 E. M. Dias and C. Petit, *J. Mater. Chem. A*, 2015, **3**, 22484–22506.
- 18 Y. Li, H. Xu, S. Ouyang and J. Ye, *Phys. Chem. Chem. Phys.*, 2016, **18**, 7563–7572.
- 19 C. Zlotea, D. Phanon, M. Mazaj, D. Heurtaux, V. Guillermin, C. Serre, P. Horcajada, T. Devic, E. Magnier, F. Cuevas *et al.*, *Dalton Trans.*, 2011, **40**, 4879–4881.
- 20 Y. Fu, D. Sun, Y. Chen, R. Huang, Z. Ding, X. Fu and Z. Li, *Angew. Chem. International Edition*, 2012, **51**, 3364–3367.
- 21 S. Kampouri, T. N. Nguyen, C. P. Ireland, B. Valizadeh, F. M. Ebrahim, G. Capano, D. Ongari, A. Mace, N. Guijarro, K. Sivula *et al.*, *J. Mater. Chem. A*, 2018, **6**, 2476–2481.
- 22 I. E. Castelli, T. Olsen, S. Datta, D. D. Landis, S. Dahl, K. S. Thygesen and K. W. Jacobsen, *Energy Environ. Sci.*, 2012, **5**, 5814–5819.
- 23 I. E. Castelli, D. D. Landis, K. S. Thygesen, S. Dahl, I. Chorkendorff, T. F. Jaramillo and K. W. Jacobsen, *Energy Environ. Sci.*, 2012, **5**, 9034–9043.
- 24 H. L. Zhuang and R. G. Hennig, *Chem. Mater.*, 2013, **25**, 3232–3238.
- 25 N. Kharche, M. S. Hybertsen and J. T. Muckerman, *Phys. Chem. Chem. Phys.*, 2014, **16**, 12057–12066.
- 26 X. Li, J. Yu, J. Low, Y. Fang, J. Xiao and X. Chen, *J. Mater. Chem. A*, 2015, **3**, 2485–2534.
- 27 V. Stevanović, S. Lany, D. S. Ginley, W. Tumas and A. Zunger, *Phys. Chem. Chem. Phys.*, 2014, **16**, 3706–3714.
- 28 J. Cheng and M. Sprik, *Phys. Rev. B*, 2010, **82**, 081406.
- 29 Y. Wu, M. Chan and G. Ceder, *Phys. Rev. B*, 2011, **83**, 235301.
- 30 J. Cheng and M. Sprik, *Phys. Chem. Chem. Phys.*, 2012, **14**, 11245–11267.
- 31 C. G. Van de Walle and J. Neugebauer, *Nature*, 2003, **423**, 626.
- 32 I. E. Castelli, J. M. García-Lastra, F. Hüser, K. S. Thygesen and K. W. Jacobsen, *New J. Phys.*, 2013, **15**, 105026.
- 33 Y. Ping, R. Sundararaman and W. A. Goddard III, *Phys. Chem. Chem. Phys.*, 2015, **17**, 30499–30509.

- 34 Z. Guo, F. Ambrosio, W. Chen, P. Gono and A. Pasquarello, *Chem. Mater.*, 2017, **30**, 94–111.
- 35 N. Kharche, J. T. Muckerman and M. S. Hybertsen, *Phys. Rev. Lett.*, 2014, **113**, 176802.
- 36 T. A. Pham, D. Lee, E. Schwegler and G. Galli, *J. Am. Chem. Soc.*, 2014, **136**, 17071–17077.
- 37 C. G. Van de Walle and R. M. Martin, *Phys. Rev. B*, 1987, **35**, 8154.
- 38 A. Baldereschi, S. Baroni and R. Resta, *Phys. Rev. Lett.*, 1988, **61**, 734.
- 39 A. Alkauskas, P. Broqvist, F. Devynck and A. Pasquarello, *Phys. Rev. Lett.*, 2008, **101**, 106802.
- 40 N. G. Hörmann, Z. Guo, F. Ambrosio, O. Andreussi, A. Pasquarello and N. Marzari, *npj Comput. Mater.*, 2019, **5**, 1–6.
- 41 K. Steiner, W. Chen and A. Pasquarello, *Phys. Rev. B*, 2014, **89**, 205309.
- 42 J. Robertson, *J. Vac. Sci. Technol. B*, 2000, **18**, 1785–1791.
- 43 J. VandeVondele, M. Krack, F. Mohamed, M. Parrinello, T. Chassaing and J. Hutter, *Comput. Phys. Commun.*, 2005, **167**, 103–128.
- 44 S. Goedecker, M. Teter and J. Hutter, *Phys. Rev. B*, 1996, **54**, 1703.
- 45 C. Hartwigsen, S. Goedecker and J. Hutter, *Phys. Rev. B*, 1998, **58**, 3641.
- 46 M. Guidon, J. Hutter and J. VandeVondele, *J. Chem. Theory Comput.*, 2010, **6**, 2348–2364.
- 47 J. VandeVondele and J. Hutter, *J. Chem. Phys.*, 2007, **127**, 114105.
- 48 J. P. Perdew, K. Burke and M. Ernzerhof, *Phys. Rev. Lett.*, 1996, **77**, 3865.
- 49 J. P. Perdew, M. Ernzerhof and K. Burke, *J. Chem. Phys.*, 1996, **105**, 9982–9985.
- 50 G. Sawatzky and J. Allen, *Phys. Rev. Lett.*, 1984, **53**, 2339.
- 51 M. Sharon, G. Tamizhmani, C. Levy-Clement and J. Rioux, *Solar Cells*, 1989, **26**, 303–312.
- 52 G. Capano, F. Ambrosio, S. Kampouri, K. C. Stylianou, A. Pasquarello and B. Smit, *J. Phys. Chem. C*, 2020, **124**, 4065–4072.
- 53 O. A. Vydrov and T. Van Voorhis, *J. Chem. Phys.*, 2010, **133**, 244103.
- 54 R. Sabatini, T. Gorni and S. De Gironcoli, *Phys. Rev. B*, 2013, **87**, 041108.
- 55 S. Nosé, *J. Chem. Phys.*, 1984, **81**, 511–519.
- 56 W. G. Hoover, *Phys. Rev. A*, 1985, **31**, 1695.
- 57 G. Miceli, S. de Gironcoli and A. Pasquarello, *J. Chem. Phys.*, 2015, **142**, 034501.
- 58 F. Ambrosio, G. Miceli and A. Pasquarello, *J. Phys. Chem. B*, 2016, **120**, 7456–7470.
- 59 M. Towler, N. Allan, N. M. Harrison, V. Saunders, W. Mackrodt and E. Apra, *Phys. Rev. B*, 1994, **50**, 5041.
- 60 S. Otani and N. Ohashi, *J. Ceram. Soc. Jpn*, 2013, **121**, 331–332.
- 61 F. U. Hillebrecht, H. Ohldag, N. B. Weber, C. Bethke, U. Mick, M. Weiss and J. Bahrtdt, *Phys. Rev. Lett.*, 2001, **86**, 3419–3422.
- 62 F. Ambrosio, Z. Guo and A. Pasquarello, *J. Phys. Chem. Lett.*, 2018, **9**, 3212–3216.
- 63 J. Cheng and M. Sprik, *Phys. Chem. Chem. Phys.*, 2012, **14**, 11245–11267.
- 64 C. G. Van de Walle and R. M. Martin, *Phys. Rev. B*, 1987, **35**, 8154–8165.
- 65 F. Devynck, A. Alkauskas, P. Broqvist and A. Pasquarello, *Phys. Rev. B*, 2011, **84**, 235320.
- 66 P. Tasker and D. Duffy, *Surf. Sci.*, 1984, **137**, 91 – 102.
- 67 P. Tasker, *Phil. Mag. A*, 1979, **39**, 119–136.
- 68 R. S. Koster, C. M. Fang, M. Dijkstra, A. van Blaaderen and M. A. van Huis, *J. of Phys. Chem. C*, 2015, **119**, 5648–5656.
- 69 E. J. Popczun, J. R. McKone, C. G. Read, A. J. Biacchi, A. M. Wiltrout, N. S. Lewis and R. E. Schaak, *J. Am. Chem. Soc.*, 2013, **135**, 9267–9270.
- 70 Q. Li and X. Hu, *Phys. Rev. B*, 2006, **74**, 035414.
- 71 J. He, Á. Morales-García, O. Bludský and P. Nachtigall, *CrystEngComm*, 2016, **18**, 3808–3818.
- 72 C. J. Cramer, *Computational Chemistry: Theories and Models*, John Wiley & Sons, Chichester, England, 2004.
- 73 S. S. Kocha, M. W. Peterson, D. J. Arent, J. M. Redwing, M. A. Tischler and J. A. Turner, *J. Electrochem. Soc.*, 1995, **142**, L238–L240.
- 74 A. J. Nozik, *Annu. Rev. Phys. Chem.*, 1978, **29**, 189–222.
- 75 J. Beach, R. Collins and J. Turner, *J. Electrochem. Soc.*, 2003, **150**, A899–A904.
- 76 I. Huygens, K. Strubbe and W. Gomes, *J. Electrochem. Soc.*, 2000, **147**, 1797–1802.
- 77 T. Mahmood, M. T. Saddique, A. Naeem, P. Westerhoff, S. Mustafa and A. Alum, *Ind. Eng. Chem. Res.*, 2011, **50**, 10017–10023.
- 78 J. Robertson and B. Falabretti, *J. Appl. Phys.*, 2006, **100**, 014111.
- 79 P. Peacock and J. Robertson, *J. Appl. Phys.*, 2002, **92**, 4712–4721.
- 80 B. Falabretti and J. Robertson, *J. Appl. Phys.*, 2007, **102**, 123703.
- 81 J. Robertson, *Appl. Surf. Sci.*, 2002, **190**, 2–10.
- 82 J. Robertson, *Phys. Status Solidi A*, 2010, **207**, 261–269.
- 83 J. Tersoff, *Phys. Rev. B*, 1984, **30**, 4874–4877.
- 84 J. Tersoff, *Phys. Rev. B*, 1985, **32**, 6968–6971.
- 85 J. Tersoff, *Phys. Rev. Lett.*, 1984, **52**, 465–468.
- 86 R. L. Andersen, *Solid-State Electron.*, 1962.
- 87 W. Mönch, *Phys. Rev. Lett.*, 1987, **58**, 1260–1263.
- 88 W. Mönch, *Surf. Sci.*, 1994, **299-300**, 928 – 944.
- 89 K. T. Butler, C. H. Hendon and A. Walsh, *J. Am. Chem. Soc.*, 2014, **136**, 2703–2706.
- 90 J. K. Nǎyrskov, J. Rossmeisl, A. Logadottir, L. Lindqvist, J. R. Kitchin, T. Bligaard and H. Jǎnsson, *J. of Phys. Chem. B*, 2004, **108**, 17886–17892.
- 91 X. Guo, J. Ji, Q. Jiang, L. Zhang, Z. Ao, X. Fan, S. Wang, Y. Li, F. Zhang, G. Zhang and W. Peng, *ACS Appl. Mater. Interfaces*,

- 2017, **9**, 30591–30598.
- 92 R. A. Marcus, *Rev. Mod. Phys.*, 1993, **65**, 599–610.
- 93 G. L. Hug and B. Marciniak, *J. Phys. Chem.*, 1995, **99**, 1478–1483.
- 94 M. Evans and M. Polanyi, *Trans. Faraday Soc.*, 1938, **34**, 11–24.
- 95 F. Ambrosio, J. Wiktor and A. Pasquarello, *ACS Appl. Mater. Interfaces*, 2018, **10**, 10011–10021.